IEEE Access
Multidisciplinary ⋮ Rapid Review ⋮ Open Access Journal

Received 1 February 2025, accepted 2 March 2025, date of publication 10 March 2025, date of current version 18 March 2025.

Digital Object Identifier 10.1109/ACCESS.2025.3549619

RESEARCH ARTICLE

Self-Isolation in MIMO Array Using Mode Diversity

MANZOOR ELAHI[1], SLAWOMIR KOZIEL[1,2], (Senior Member, IEEE), AND LEIFUR LEIFSSON[3]

[1]Engineering Optimization and Modeling Center, Reykjavik University, 102 Reykjavik, Iceland
[2]Faculty of Electronics, Telecommunications and Informatics, Gdańsk University of Technology, 80-233 Gdańsk, Poland
[3]School of Aeronautics and Astronautics, Purdue University, West Lafayette, IN 47907, USA

Corresponding author: Slawomir Koziel (koziel@ru.is)

This work was supported in part by Icelandic Research Fund under Grant 239858, and in part by the National Science Centre of Poland under Grant 2022/47/B/ST7/00072.

ABSTRACT A new isolation technique is proposed for multiple-input multiple-output (MIMO) microstrip patch antenna (MPA) arrays utilizing mode diversity. Typically, similar modes are excited in each element of the MIMO array. However, the proposed MIMO array uses two elements of different sizes excited in distinct modes at the same frequency. It is found that the TM_{01} mode excited in one MPA, a hybrid mode ($TM_{03} + TM_{21}$) is induced in the coupled MPA, while exciting the TM_{03} mode in another patch induces a quasi-TM_{11} mode in the coupled MPA. Both induced modes exhibit weak fields at the feeding points, reducing the mutual coupling between the two patch antennas without requiring extra decoupling structure. Additionally, the induced modes create a null in the broadside direction, reducing cross-polarization (x-pol) levels. An isolation level over 50 dB is achieved in 1×2 MIMO array at 5.8 GHz. The design is adaptable to larger array. Therefore, to validate the design technique, a 1×4 array is simulated, fabricated and measured, showing 30–45 dB isolation among the ports in the passband. Moreover, the design features an x-pol around -40 dB in broadside direction in both E- and H-planes, ensuring effective polarization diversity. The technique is applied to a MIMO dielectric resonator antenna (DRA) array, demonstrating excellent isolation and radiation pattern performance. Furthermore, the technique is versatile and can be applied to various MIMO configurations. Therefore, simulations have been performed for 2×4 MPA array, validating the effectiveness of isolation in both the E- and H-planes. This approach also optimizes space utilization, allowing for the inclusion of additional patch elements to form hybrid-coupled MIMO MPAs within confined spaces.

INDEX TERMS Microstrip patch antenna, multiple-input multiple-output, isolation, self-decoupling method, mode's diversity, cross-polarization.

I. INTRODUCTION

MIMO technology, with its potential to improve channel capacity and the transmission rate without extra spectrum resources [1], [2], has the ability to boost communication system performance significantly. However, limited space for MIMO antennas often results in significant mutual coupling between antenna elements, causing impedance matching and radiation performance issues and reducing the communication quality of the wireless system as a whole [3], [4]. Therefore, the issue of decreasing antenna mutual coupling has gained notable interest and has become a trending research field [5], [6].

MPAs provide many advantages, such as a planar layout, small size, lightweight, and simple integration with other circuits [7]. These benefits make them appropriate for extensive use in wireless communication systems.

Various methods have been proposed to address the problem of coupling in MIMO antenna systems [8], [9],

The associate editor coordinating the review of this manuscript and approving it for publication was Santi C. Pavone.

[10], [11], [12], [13], [14], [15], [16], [17], [18], [19], [20], [21]. Using the defected ground structure (DGS) [8], [9], electromagnetic bandgap structure (EBG) [10], and complementary split ring resonators (CSRR) [11] are among possible methods. These techniques reduce the coupling between MIMO antenna elements by introducing additional structures between them, preventing transmission. Other approaches create additional coupling paths to counteract the impact of the original coupling path, achieved through neutralization lines [12], [13], loading aperture [14], and parasitic elements [15], [16], [17], [18]. Additionally, the research in [19], [20], and [21] suggests metasurfaces and near-field resonators to reduce mutual coupling by canceling both coupled and reflected waves. While these techniques successfully minimize mutual coupling, they frequently necessitate additional horizontal or vertical space, leading to a considerable increase in system size and complexity. Furthermore, these configurations may negatively impact the radiation properties of the antenna.

To overcome these shortcomings, self-decoupling techniques have been receiving a lot of attention as they do not require additional decoupling structures [22], [23], [24], [25], [26], [27], [28], [29], [30], [31], [32]. Instead, they rely on the antenna's intrinsic characteristics. The techniques consist of canceling modes [22], [23], using out-of-phase modes [24], adding lumped element capacitors on the ground plane [25], [26], creating nulls at the feed point [27], utilizing higher-order modes [28], using characteristic modes on the ground [29], employing orthogonal mode pairs [30], [31], and field redistribution method [32].

This manuscript proposes a new self-decoupling technique to suppress the mutual coupling between the MPAs in a MIMO array. Different from the existing decoupling methods, this self-isolation technique utilizes mode diversity to excite the fundamental TM_{01}-mode in one MPA and a higher-order TM_{03} mode in the other MPA of the MIMO antenna, operating at the same resonant frequency. The elements are arranged such that the excited TM_{03} mode in one MPA generates a TM_{11} mode in the non-excited patch. Similarly, the excited TM_{01} mode induces a hybrid mode (superposition of TM_{03} and TM_{21}) in the non-excited MPA. All these coupled modes exhibit nulls in the broadside direction. A 1×2 MIMO array is designed at 5.8 GHz that achieved an isolation of more than 50 dB. Moreover, this method is extended to larger arrays. Therefore, the proposed design technique has been demonstrated by experimental validation of 1×4 MIMO structure. The measured results showed a good agreement with the simulated results. An isolation of 30 to 45 dB is achieved among the ports in the passband and a reduced x-pol of 40 dB is observed in the broadside direction in both E- and H-planes, which is a desired factor in the MIMO antennas. Thus, the proposed MIMO array has broad applications in MIMO systems. The technique is applied to the MIMO DRA to demonstrate its versatility, achieving an isolation of 45 dB at the resonant frequency and x-pol levels of -30 dB in the $\phi = 0°$ and $\phi = 90°$

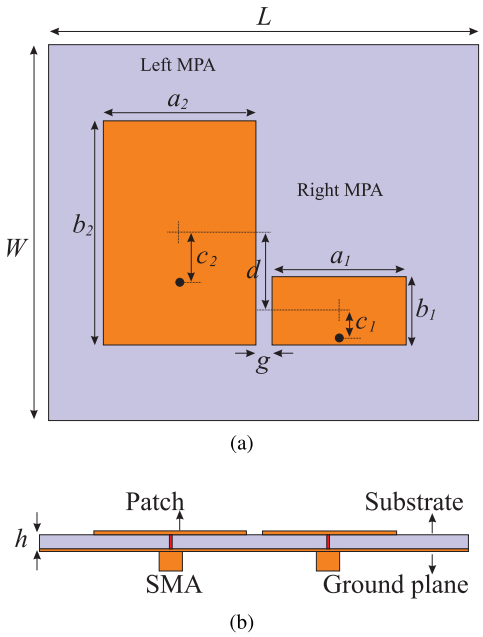

FIGURE 1. Geometry of the proposed MIMO antenna array: (a) top view. (b) cross-sectional view. $[L = 80, W = 70, a_1 = 25, b_1 = 13, a_2 = 27.5, b_2 = 41, c_1 = 5, c_2 = 11, d = 14, g = 2, h = 1.524]_{mm}$.

planes. The proposed technique offers several advantages. It can be applied to larger n^{th}-order array (where $n = 1, 2, 3, \ldots$). For instance, a 2×4 MIMO MPA array was simulated to verify scalability, achieving isolation greater than 22 dB among the ports. Furthermore, the technique provides flexibility in implementing MIMO arrays without being restricted to symmetrical structures, relying solely on operating modes. This approach intrinsically reduces the size of one patch, saving space that can be used for additional elements. For example, a six-port compact hybrid-coupled MIMO MPA array was simulated, offering isolation of greater than 23 dB across the bandwidth. As this approach is frequency-specific and relies on precise mode excitation without using additional decoupling structure, it shows excellent performance in narrowband MIMO arrays. However, the self-isolated wideband MIMO array has yet to be investigated.

II. DESIGN OF THE MPA MIMO ARRAY

The configuration of the proposed 1×2 MPA MIMO array is illustrated in Fig. 1. The MPAs of dimensions $a_1 \times b_1$ and $a_2 \times b_2$ are printed on the top layer of single-layer dielectric substrate (1.524 mm thick Rogers RO4003C, $\epsilon_r = 3.38$) separated by a distance g. The ground is fabricated on the bottom layer of the substrate. A 50 Ω coaxial probe feeds both MPAs. The positions of the probes are adjusted such that the fundamental TM_{01}-mode is excited in the right MPA of size $a_1 \times b_1$, and the higher-order TM_{03}-mode is effectively excited in the left MPA of size $a_2 \times b_2$, operating at the same frequency, 5.8 GHz. The detailed dimensions are listed in the caption of Fig. 1.

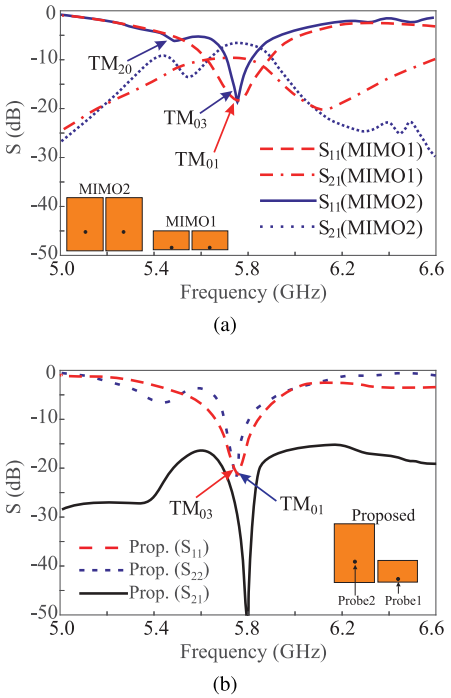

FIGURE 2. Simulated *S*-parameters of: (a) MIMO1 and MIMO2, (b) proposed MIMO antenna array.

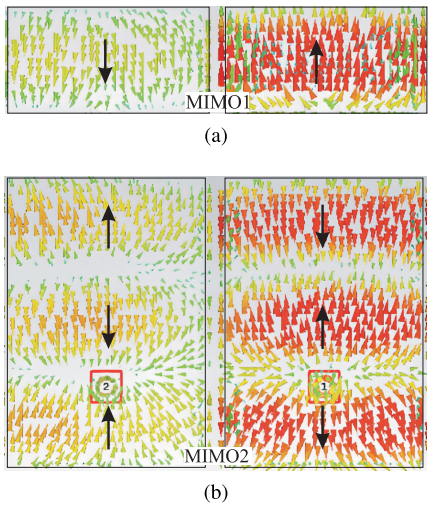

FIGURE 3. Simulated current distribution on MIMO antenna arrays at 5.8 GHz: (a) MIMO1, (b) MIMO2.

A. DECOUPLING MECHANISM

As depicted in Fig. 1, the absence of an extra decoupling structure in MIMO array indicates the significant impact of the modes in each MPA on isolation enhancement. To illustrate the isolation technique, three MPA MIMO configurations were created at 5.8 GHz. The first configuration had both elements activated with a fundamental TM_{01} mode (MIMO1), and another configuration with higher-order TM_{03} mode (MIMO2). Finally in the proposed MIMO, different modes are excited in each element: fundamental TM_{01} mode in the right MPA and higher-order TM_{03} mode in the left MPA. From the cavity model of the patch antenna,

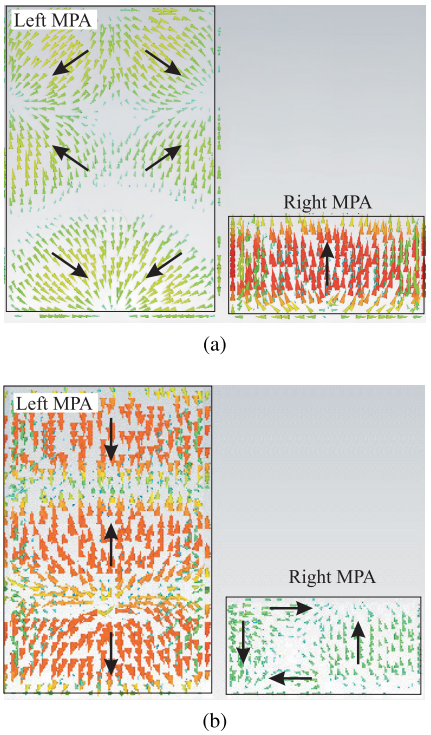

FIGURE 4. Simulated current distributions on proposed MIMO array at 5.8 GHz: (a) right MPA excited with TM_{01}-mode, (b) left MPA excited with TM_{03}-mode.

the TM_{mn} mode refers to a specific transverse magnetic mode characterized by its field distribution across the patch dimensions, whose resonant frequency is given by [33]:

$$f_{mn} = \frac{c}{2}\sqrt{\left(\frac{m}{W}\right)^2 + \left(\frac{n}{L}\right)^2}\frac{1}{\sqrt{\epsilon_r}} \tag{1}$$

where m and n are the number of half-wave variations along the length of the patch, c is the speed of light, W is the width of the patch, L length of the patch along which the E-field has sinusoidal distribution, and ϵ_r is the dielectric constant of the substrate. Based on Eq (1), the dimension of a single element of MIMO1 is $a_1 \times b_1 = 25mm \times 14\ mm$ and that of MIMO2 is $a_2 \times b_2 = 25\ mm \times 41.5\ mm$ at 5.8 GHz. These dimensions are slightly adjusted to achieve the desired results for the proposed MIMO array.

Fig. 2(a) illustrates the comparison of *S*-parameters for the MIMO1 and MIMO2 arrays. In the case of MIMO1, the resonance appears at 5.8 GHz. Both MPAs exhibit low isolation of 12 dB at the operating frequency. In MIMO2, both MPAs are excited at 5.8 GHz with the higher-order TM_{03} mode. The mutual coupling remains high, at approximately −8 dB. However, in the proposed configuration, the right and left MPAs are excited with the TM_{01} and TM_{03} modes, respectively, achieving remarkable isolation of >50 dB, as shown in Fig. 2(b). For additional analysis, the simulated current distributions on the MPAs of the MIMO1 and MIMO2 are presented in Fig. 3. Since the decoupling effect is observed only at 5.8 GHz, the subsequent comparison will

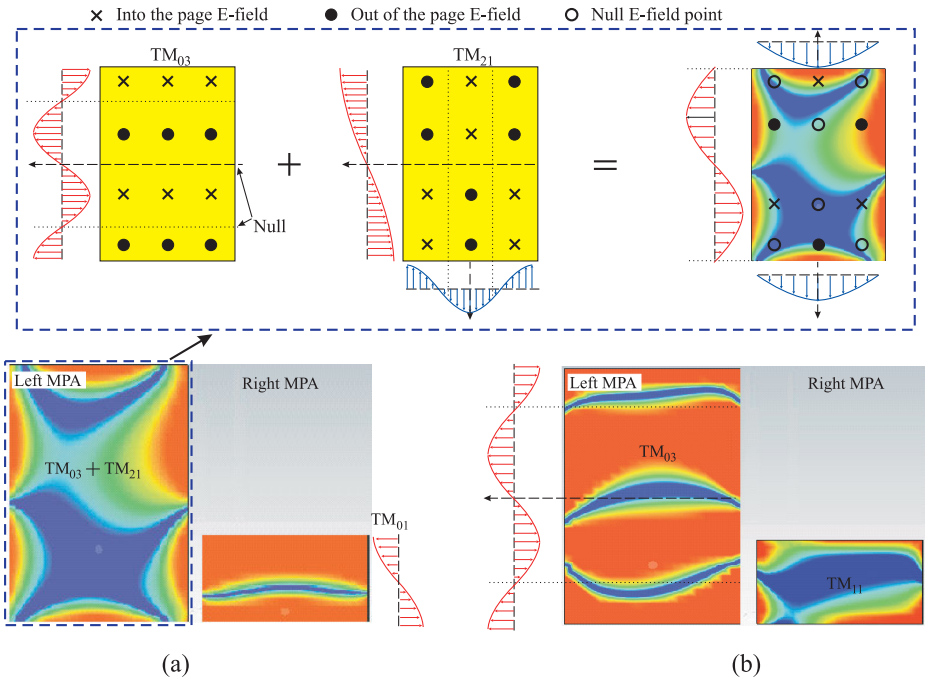

FIGURE 5. Simulated E-field distribution on the proposed MIMO array at 5.8 GHz: (a) right MPA excited, (b) left MPA excited.

focus solely on this frequency. During the simulation, the right MPA is excited, while the left MPA is terminated with a 50 Ω load. As shown in Fig. 3(a), the TM_{01} mode is activated in the right MPA of the MIMO1 array. Due to mutual coupling, the left MPA also exhibits the induced TM_{01} mode, leading to significant mutual coupling of −12 dB. Similarly, the right MPA of MIMO2 excites the higher-order TM_{03} mode, which is also coupled to the left MPA, as shown in Fig. 3(b), resulting in mutual coupling of −8 dB at the resonance frequency.

Exciting these different modes at the same frequency individually in different elements of the MPA MIMO array boosts isolation to more than 50 dB in the proposed design. Fig. 4 assists in understanding the isolation phenomena in MPAs of the proposed MIMO array by showing the current distribution. In Fig. 4(a), the right MPA is activated, and the left MPA is connected to a 50 Ω termination. The right MPA is operating with the TM_{01} mode with the current distribution displayed at 5.8 GHz. The coupled mode in the left MPA is the superposition of the TM_{03} and TM_{21} modes that do not radiate properly in the broadside direction and create a null region at the feeding point. In the same way, when the left MPA is simulated with the TM_{03} mode, as seen in Fig. 4(b), the currents on the coupled right MPA create a null region at the feeding point which is related to the TM_{11} mode. From the above illustration, the coupled currents are either orthogonal to the excited currents in the active MPA or having an overall null effect in both cases. As a result, isolation is greatly improved in the proposed structure. Another advantage of this method is that it decreases x-pol radiation at the desired frequency due to the creation of a null in the broadside direction of the coupling mode. For further illustration, Fig. 5 shows the equivalent E-field distribution in the proposed MPA MIMO array is simulated at 5.8 GHz. Fig. 5(a) clearly shows that how the coupled mode in the left MPA is the result of the superposition of the TM_{03} and TM_{21} modes. Similarly, TM_{11} mode is induced in the right MPA by the exciting the TM_{03} mode in the left MPA. All these field distributions align well with their current distributions given in Fig. 4.

B. PARAMETRIC STUDY

This section consists of a parametric study of certain parameters to characterize the decoupling method. Fig. 6(a) depicts how the gap between the elements influences the results. When changing the gap g from 2 to 5 mm, it is evident that the resonance frequency of TM_{01} and TM_{03} remains constant at 5.8 GHz, with minor changes in the impedance matching levels $\min|S_{11}|$ and $\min|S_{22}|$, as predicted since g is unrelated to these factors. Nevertheless, the minimum absolute value of $\min|S_{21}|$ is significantly impacted. As demonstrated, the decrease in $\min|S_{21}|$ outside of the band increases with the increase of g, consistent with the conventional understanding that the smaller the spacing, the stronger the resulting coupling. The optimal S_{21} in the passband is achieved for $g = 3$ mm. The noticeable difference in the isolation level is due to the varying field intensity levels caused by different spacings. Another parameter, d, adversely affects the isolation, as depicted in Fig. 6(b). Reducing d from 14.5 mm to 0 mm significantly increases mutual coupling

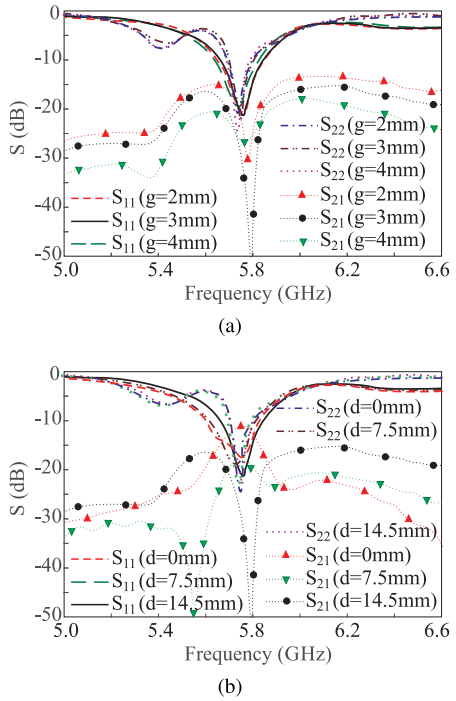

FIGURE 6. Simulated *S*-parameters of the proposed MPA array for different: (a) spacings g between the MPAs, (b) vertical position d of the right MPA.

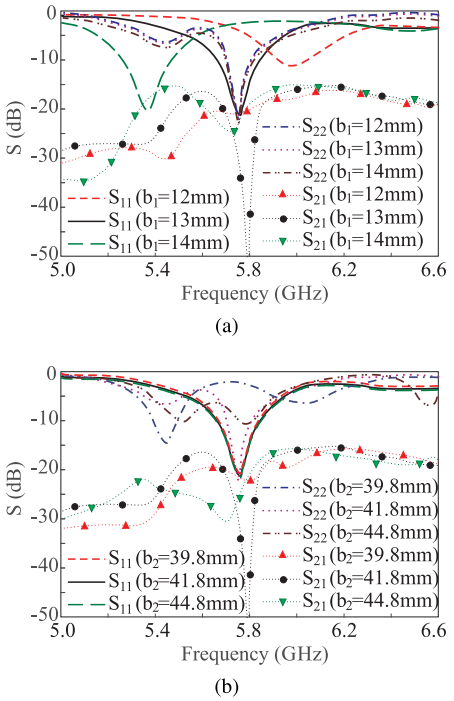

FIGURE 7. Simulated *S*-parameters of the proposed MPA array for different: (a) lengths b_1 of the right MPA, (b) lengths b_2 of the left MPA.

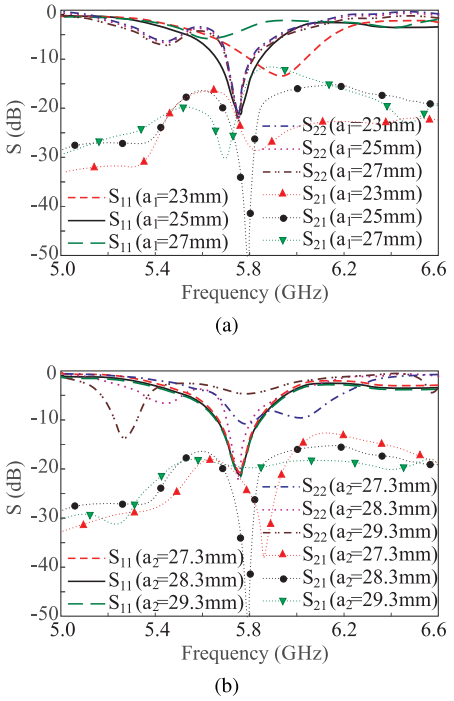

FIGURE 8. Simulated *S*-parameters of the proposed MPA array for different: (a) widths a_1 of the right MPA, (b) widths a_2 of the left MPA.

to −12 dB, along with noticeable changes in $|S_{11}|$ matching and resonance. Nevertheless, there is no apparent alteration in $|S_{22}|$ matching and resonance. The observed differences in $|S_{11}|$ can be explained as follows. In principle, the TM_{03} mode has three currents along the length of the MPA with alternating directions, whereas the TM_{01} mode has only one current. Each current can be considered a separate source for ease of understanding in this specific case. When $d = 0$, the right MPA becomes horizontally aligned with the left MPA's center. Therefore, at this location, the current on the right MPA is susceptible to the collective impact of the three currents on the left MPA. This influences both resonance and matching. The current on the right MPA has little effect on the three current sources, resulting in insignificant changes in both the matching and resonance of S_{22}. Regarding S_{21}, the currents on the right MPA are closer to the three currents at $d = 0$ mm compared to the right MPA placed at $d = 14.5$ mm in this specific configuration. Therefore, when $d = 0$ is varied, the coupled field intensities in both MPAs change accordingly. As a result, the coupled field at the feeding position is also altered. Once the field intensity at the feeding position approaches zero, optimal isolation can be achieved. Here, the optimal value of d is 14.5 mm.

Figs. 7 and 8 present a parametric study focused on the sensitivity of the resonant modes to the patch dimensions. These studies reveal how changes in the patch dimensions influence the resonant modes of each patch. The effects of the patch lengths b_1 and b_2 on the resonant frequencies of the TM_{01} and TM_{03} modes are shown in Figs. 7(a) and 7(b), respectively. Variations in b_1 of the right patch change the resonant frequency of TM_{01} modes, without influencing the TM_{03} mode of the left patch. Similarly, changes in b_2 exclusively impact the TM_{03} mode. At $b_2 = 41.8$ mm, the left patch effectively resonates at 5.8 GHz

with the TM_{03}, while the TM_{02} mode at 5.4 GHz remains unmatched. Reducing b_2, shifts the TM_{03} mode to the higher frequency of 5.92 GHz with reduced matching, and slightly shifts the TM_{20} mode to 5.43 GHz, where good matching is achieved. Conversely, increasing b_2 disrupts the matching of the TM_{03} mode, although frequency remains near 5.8 GHz. The TM_{20} mode gets closer to the TM_{03} mode. Additionally, a higher-order mode emerges at 6.58 GHz. These dimensional variations significantly degrade isolation performance, which can be attributed to changes in the field distributions on the patch. The altered dimensions misalign the null locations with the feed points, negatively impacting the design's overall performance. However, the isolation remains above 20 dB, indicating that isolation is not signinficantly affected by minor variations in patch dimensions during fabrication. This is due to a wide null region around the feed point.

Before conducting a parametric study on the widths of the MPAs, it is essential to note that the MPA widths do not directly determine the resonant frequencies of the operating modes (TM_{01} and TM_{03}) as described by (1). Instead, they primarily influence the input impedance, bandwidth, and radiation efficiency. However, the widths indirectly affect the resonant frequencies through their impact on the effective dielectric constant of the antenna system. Fig. 8 illustrates the influence of MPA widths on the resonant frequencies of the modes. Adjusting the width a_1 of the right MPA affects only the resonant frequency of the TM_{01} mode, resulting in reduced matching, with no changes in the TM_{03} resonance. Similarly, varying a_2 impacts only the TM_{03} mode. A shift in the TM_{20} mode to a lower frequency is observed, along with degraded matching of the TM_{03} mode at 5.8 GHz and the appearance of an additional mode at 6.59 GHz. Conversely, when a_2 is decreased, the TM_{20} and TM_{03} modes shift to higher frequencies. The degraded isolation performance can be attributed to field redistribution on the patches, causing misalignment between the null field point and the feed point.

From the parametric analysis, it is evident that the operating modes of the MPAs can be tuned to specific frequencies by adjusting the patch dimensions. Furthermore, the resonant frequency of each mode is independent, meaning that altering the dimensions of one MPA does not affect the resonant frequency of the other. However, effective isolation between the patches can be achieved by carefully selecting the lengths and widths of the MPAs, ensuring that the field distribution on each element is configured to create a null at the feed point of the coupled MPA.

Following a thorough description of the sensitivity of the MIMO antenna system, it is essential to mention the fabrication tolerance, particularly concerning patch dimensions and other design parameters and its effect on the performance of the MIMO array. The proposed design demonstrates robustness against fabrication tolerances, including variations in substrate thickness and etching precision. The presence of a wide null around the feeding points of the coupled patches ensures that isolation remains largely unaffected by such tolerances. Moreover, parametric studies indicate that

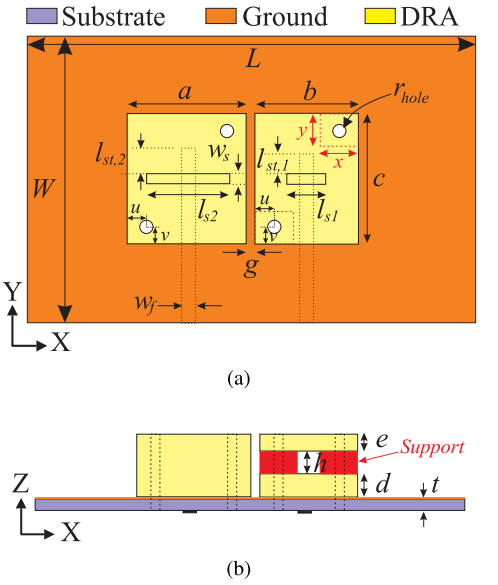

FIGURE 9. Geometry of the proposed MIMO DRA: (a) top view. (b) side view. $[a = 28.5, b = 24.4, c = 31.55, d = 6, e = 4.03, g = 2, h = 5.92, l_{s1} = 9.4, l_{s2} = 20.13, w_s = 2, l_{st1} = 7.45, l_{st2} = 6.2, w_f = 3.34, t = 1.524, u = 4.2, v = 3.77, x = 8, y = 8, r_{hole} = 1.3, L = 110, W = 70]_{mm}$.

isolation remains above 20 dB at 5.8 GHz even when the length and width of the MPAs vary by up to 2 mm, which is a large margin for state-of-the-art fabrication facilities. Furthermore, the Rogers RO4003C substrate, with a dielectric constant of 3.38±0.05, and a thickness of 1.52±0.05 mm, was chosen for its low variability in dielectric properties and thickness, ensuring minimal impact on electrical performance of the MIMO array. Additionally, the RO4003C substrate is less susceptible to environmental variations due to its low thermal coefficient of dielectric constant and resistance to moisture, maintaining stable dielectric properties under varying humidity and temperature conditions. Additionally, the integration of the MIMO antenna with a wireless system or other devices could affect its performance, including mismatching, isolation, and radiation characteristics. Therefore, some optimization can be done to achieve the desired results while considering the integrated system. In some scenarios, the configuration of the MIMO antenna elements may need to be adjusted. However, the main focus of this manuscript is to highlight the efficacy of the proposed isolation method, which can be applied to other designs for specific wireless systems.

III. DESIGN OF THE MIMO DRA

As discussed earlier, the proposed technique is mode-specific and does not rely on the radiator. Therefore, it applies to other types of antennas. For demonstration, a 1 × 2 MIMO DRA is designed in this section at 5.2 GHz instead of 5.8 GHz, where the MIMO patch array was implemented to showcase the flexibility and adaptability of the proposed mode diversity technique. This choice highlights the generalizability of the technique across different frequency bands and antenna types.

Fig. 9 illustrates the geometry of the proposed MIMO DRA array. Two dissimilar dielectric resonators (DRs) made of alumina ($\epsilon_r = 9.9$, $\tan\delta = 0.0001$) are mounted on the ground plane and fed by microstrip lines printed on the bottom layer of the Taconic RF−35 ($\epsilon_r = 3.5$, $\tan\delta = 0.0025$) substrate through rectangular slots etched into the ground plane on the top layer. The left DR is a single cube that excites a higher-order quasi-TE_{113} mode, whereas the right DR comprises two slabs with a vertical air gap h, exciting the fundamental mode, TE_{111}, at the operating frequency of 5.2 GHz. Two distinct DRAs with different excited modes at the same frequency lead to variations in the remaining design parameters. The DRA dimensions for a specific mode at a given resonance frequency are derived from the transcendental equations [34]:

$$k_x = \frac{\pi}{a}, k_y = \frac{\pi}{b}, {k_x}^2 + {k_y}^2 + {k_z}^2 = \epsilon_r {k_0}^2 \quad (2)$$

$$k_z tan(k_z \frac{c}{2}) = \sqrt{(\epsilon_r - 1){k_0}^2 - {k_z}^2} \quad (3)$$

where k_x, k_y, and k_z are the wavenumbers along the x–, y–, and z–axis, respectively. For a given parameter of the DRA ϵ_r, a, b, and c, the resonance frequency is the one at which the wavenumber k_z, determined using the (1) also satisfies (2). Based on these equations, the initial dimensions of the left DRA (L-DRA) and right DRA (R-DRA) were selected to resonate with their respective modes at 5.2 GHz. Subsequently, the design was optimized to account for mutual coupling, with the final dimensions provided in the caption of Fig. 9, which are slightly different from the initial parameters. The R-DRA consists of two parts: the first DRA, in contact with the ground, predominantly excites the fundamental mode, while the second DRA, positioned at a height h above the first with the help of a support made of plastic material, acts as a superstrate. This superstrate directs the energy in the broadside direction and does not contribute to the excitation of the fundamental mode. Without this arrangement, a tilted beam would result due to the unequal dimensions of the DRAs. To ensure a firm contact between the ground and the DRs, air holes of radius r_{hole} are drilled in the DRs as well as the substrate for the polycarbonate screws [35].

A. DECOUPLING MECHANISM

No additional decoupling structure in MIMO DRA indicates that the modes in each DRA play a critical role in improving isolation. For demonstration, three different MIMO DRAs were designed at 5.2 GHz: one with both elements excited in the fundamental TE_{111} (MIMO1), another with both elements excited in the quasi-TE_{113} mode (MIMO2), and the proposed MIMO design, where different modes were excited in each element (i.e., the TE_{111} mode in the R-DRA and the quasi-TE_{113} mode in the L-DRA). A comparison of the S-parameters of the three MIMO DRA arrays is shown in Fig. 10. For MIMO1, resonance is observed at 5.2 GHz. Analyzing the field distribution inside the DRA confirms that the mode is the fundamental TE_{111}. However, the two DRA elements exhibit low isolation, achieving only 12 dB in the band. Similarly, in MIMO2, where both DRAs are excited in the quasi-TE_{113} mode at 5.2 GHz, the isolation remains at the same level. In contrast, the proposed structure, with the L- and R-DRAs excited in the quasi-TE_{113} and TE_{111} modes, respectively, achieves an impressive isolation of 40 dB.

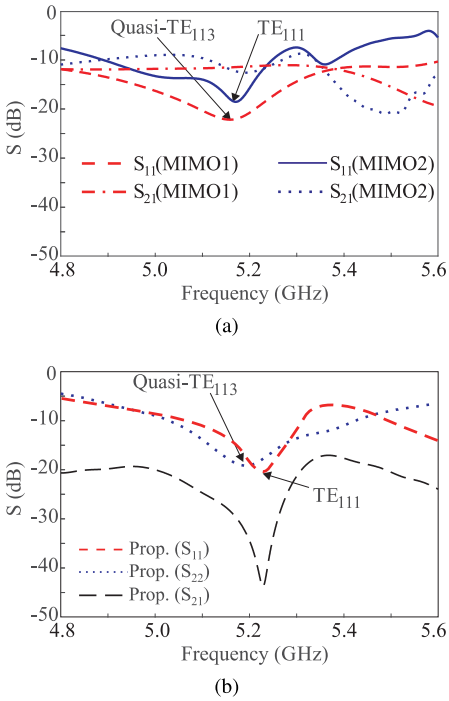

FIGURE 10. Simulated *S*-parameters: (a) MIMO1 and MIMO2, (b) Proposed MIMO.

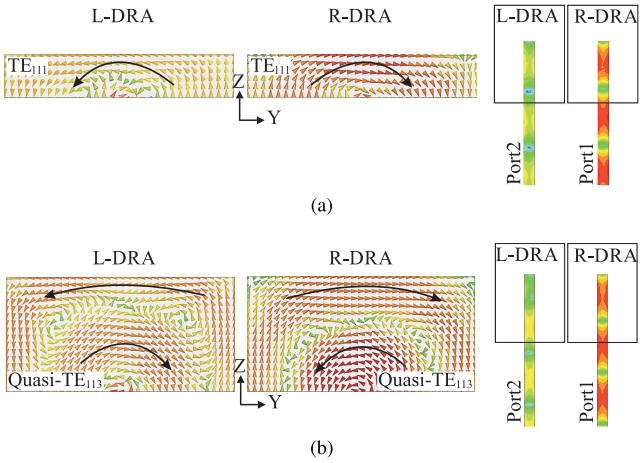

FIGURE 11. Simulated E-field inside the DRAs and Current intensity on the feedlines at 5.2 GHz: (a) MIMO1, (b) MIMO2.

To investigate the isolation mechanism further, the simulated E-field distributions inside the DRA and the current intensities on the feedlines are shown in Fig. 11 for both MIMO1 and MIMO2. Since the decoupling effect is occurs only at 5.2 GHz, the following comparison focuses exclusively on this frequency. During simulation, the R-DRA is excited, while the L-DRA is terminated with a 50 Ω load.

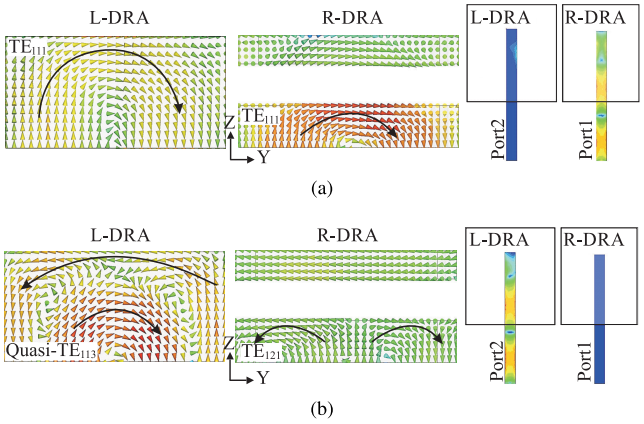

FIGURE 12. Simulated E-field inside the DRAs and Current intensity on the feedlines of the proposed MIMO DRA at 5.2 GHz: (a) TE_{111}-mode excited in R-DRA with L-DRA terminated at 50 Ω. (b) Quasi-TE_{113}-mode excited in L-DRA with R-DRA terminated at 50 Ω.

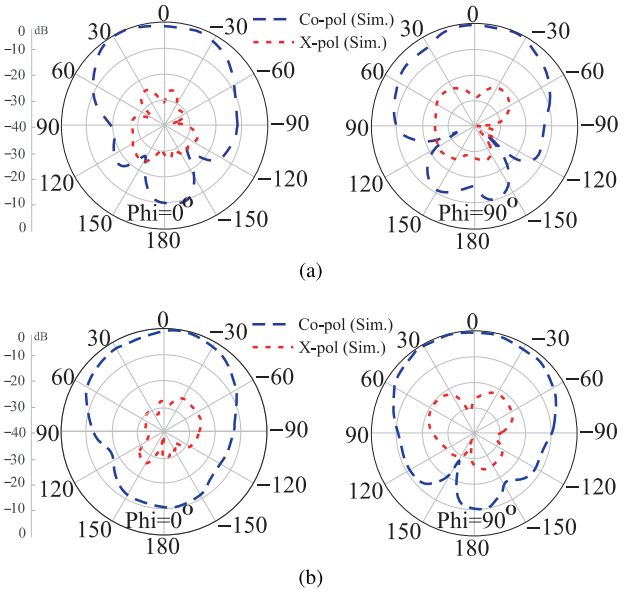

FIGURE 13. Simulated radiation patterns of the MIMO DRA array in $\phi = 0°$ and $\phi = 90°$ planes: (a) Port 1, (b) Port 2.

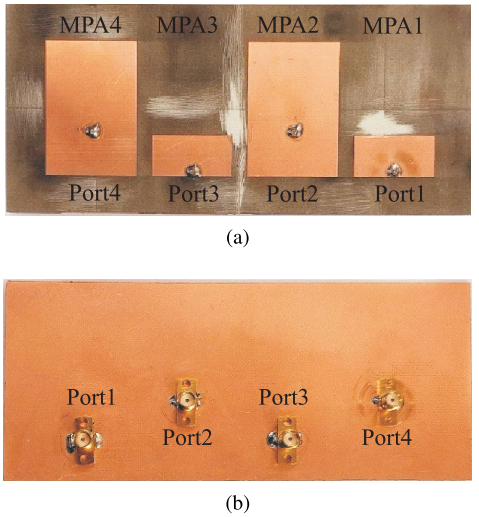

FIGURE 14. Prototype of the 1 × 4 MIMO array: (a) top layer, (b) bottom layer.

As depicted in Fig. 11(a), the TE_{111} mode is excited in the R-DRA of the MIMO1 array. Due to mutual coupling, the TE_{111} mode is also induced in the non-excited L-DRA, resulting in considerable current intensity on the microstrip feedline terminated with 50 Ω. This leads to a high coupling of −12 dB. Similarly, a higher-order quasi-TE_{113} mode is excited in the R-DRA of MIMO2 and coupled into the non-excited L-DRA, resulting in a mutual coupling of −13 dB at the resonance frequency. This is evident from the current intensity on the 50 Ω microstrip feedline, as shown in Fig. 11(b). The E-field distribution inside the DRAs of the proposed MIMO design is illustrated in Fig. 12. In Fig. 12(a), the R-DRA is excited while the L-DRA is terminated with 50 Ω. The R-DRA operates in the TE_{111} mode, with the field distribution shown at 5.2 GHz. Although the natural resonance frequency of the TE_{111} mode is 4.9 GHz, it shifts to 5.2 GHz due to the loading effect of the slot (l_{s1}=9.4 mm), which is slightly smaller than the quarter-wavelength ($\lambda_g/4$= 11.2 mm) at 5.2 GHz. The mode coupled in the L-DRA is also a fundamental TE_{111} mode. However, its operating frequency is 2.35 GHz, which is out of the band. Consequently, no energy is coupled from the R-DRA to the L-DRA at 5.2 GHz, resulting in minimal current intensity on the feedline of the non-excited DRA. The top R-DRA couples fields with the bottom R-DRA to direct radiation in the broadside direction but does not play a significant role in mode excitation. The primary radiation and mode excitation are achieved through the bottom R-DRA. In Fig. 12(b), the L-DRA is excited while the R-DRA is terminated with 50 Ω. The radiating quasi-TE_{113} mode in the L-DRA operates at 5.2 GHz and induces a TE_{121} mode in the bottom R-DRA instead of the TE_{113} mode. Since the TE_{121} mode has a null at the slot location, no energy is coupled to the R-DRA. It has been clearly demonstrated in [36] that when a slot is centrally located beneath the DRA, a TE_{pqr} mode can only be excited if all indices p, q, and r are odd numbers. Modes with even indices cannot be excited. Consequently, the fields of such modes cannot further couple to Port 2, according to the reciprocity theorem. As a result, an isolation level of 45 dB is achieved between the MIMO elements. Fig. 13 shows the radiation patterns of the MIMO DRA array for Port 1 and Port 2 in the $\phi = 0°$ and $\phi = 90°$ planes. The x-pol levels for both ports in both planes are approximately 30 dB lower than the co-polarization (co-pol) levels, validating the polarization diversity of the MIMO DRA array.

IV. EXPERIMENTAL RESULTS AND DISCUSSION

To validate the proposed technique, a 1 × 4 MIMO MPA array was designed by duplicating the discussed 1 × 2 MIMO array. The parameters match those specified in the caption of Fig. 1. Fig. 14 shows a photograph of the fabricated prototype.

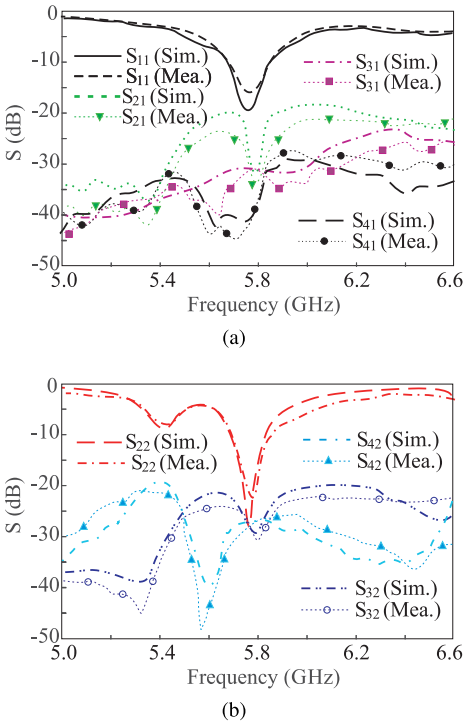

FIGURE 15. Comparison of simulated and measured *S*-parameters of 1 × 4 MIMO array: (a) Port 1, (b) Port 2.

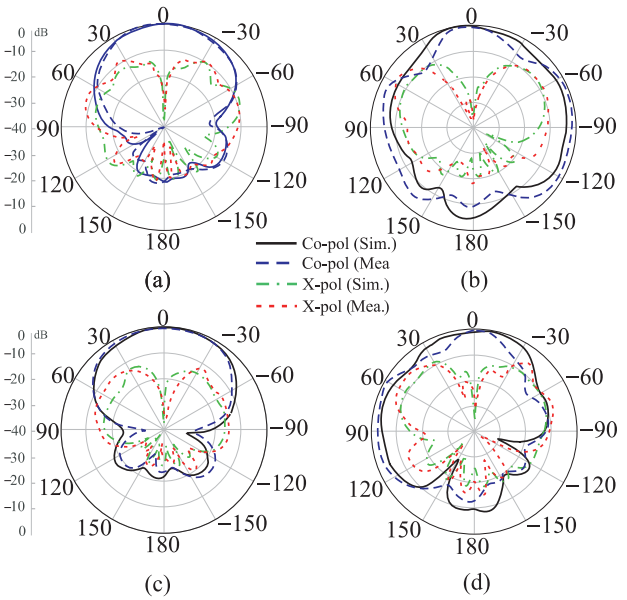

FIGURE 16. Comparison of simulated and measured radiation patterns at 5.8 GHz in $\phi = 0°$ plane: (a) Port1, (b) Port 2, (c) Port 3, and (d) Port 4.

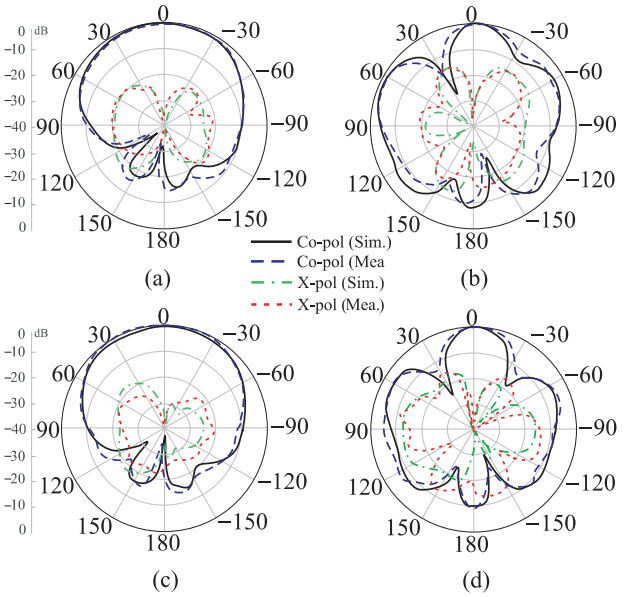

FIGURE 17. Comparison of simulated and measured radiation patterns at 5.8 GHz at $\phi = 90°$ plane: (a) Port1, (b) Port 2, (c) Port 3, and (d) Port 4.

In Fig. 15, the simulated *S*-parameters of the design are compared with the measured ones. Results from only two ports were measured for demonstration, which aligned with the simulation results. The antenna shows good performance regarding port isolation at 5.8 GHz, which varies from 30 dB to 45 dB in the passband among the ports. The isolation between Port 2 and 4 is lower than that between Port 1 and 3 due to the geometry of the 1 × 4 array. The size of MPA2 more effectively hinders the coupling fields between Port1 and Port2 as compared to the smaller MPA3 between Port 2 and Port 4. Nevertheless, the isolation is satisfactory from the perspective of MIMO array operation.

Figs. 16 and 17 illustrate the radiation characteristics of the four ports in both the $\phi = 0°$ and $\phi = 90°$ planes, respectively. The simulated and measured results are well aligned. Furthermore, the $\phi = 0°$ plane radiation patterns of Port 2 and Port 4 display two side lobes that align with the intended TM_{03} modes on them. In addition, all components effectively radiate in the broadside direction. The x-pol level of each port is low which can be attributed to the current and E-field distribution on MPAs, as demonstrated in Fig. 4 and Fig. 5. When a single element is excited, the induced currents established on the non-excited element are arranged in such a way that cancel the overall effect, resulting in a null in the broadside direction and not contributing effectively to the x-pol radiations. Fig. 18(a) depicts the farfield measurement setup. For the calibration and measurement, a three antenna-setup has been utilized as detailed in [37]. The performance of the MIMO antenna in terms of the realized gain is shown in Fig. 18(b). The measurements for two ports are given only. The broadside realized gain in the passband is around 6 dB at 5.8 GHz for Port 1 and a slightly higher gain of 6.7 dB for Port 2, which makes sense that higher-order modes usually results in a high gain. Figs. 19(a) and (b) present the simulated ECC and diversity gain (DG) based on the radiated fields for Port1 and Port2, respectively, with other ports. Typically, the ECC should not exceed 0.5 when using MIMO technology. The simulated ECC for both ports is below 0.00001 in the passband, indicating that the DG is nearly 10, which satisfies

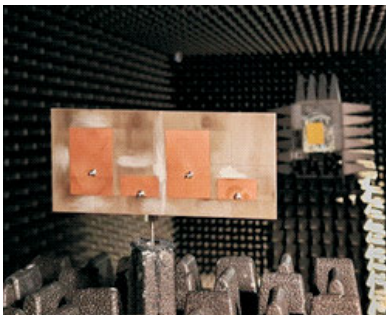

(a)

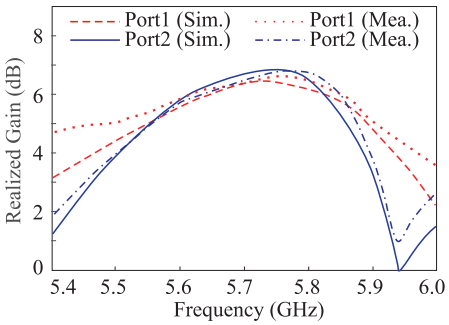

(b)

FIGURE 18. (a) Farfield measurement environment, (b) comparison of simulated and measured farfield broadside realized gain of Port 1 and Port 2.

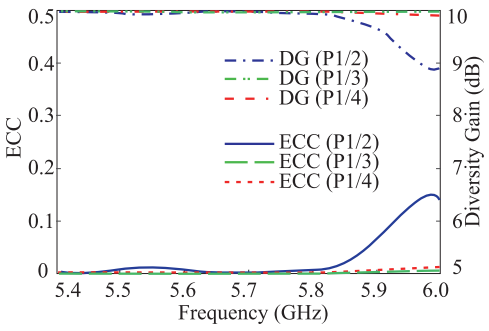

(a)

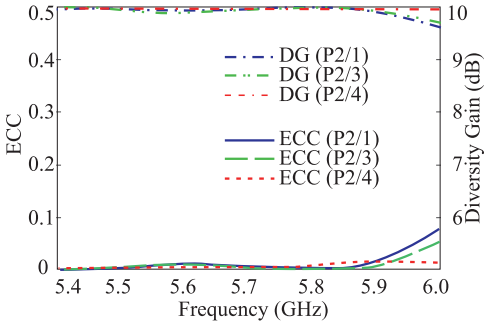

(b)

FIGURE 19. Simulated ECC and diversity gains from the radiated fields (a) Port1, (b) Port 2.

the relation between the ECC and DG given by the equation:

$$DG = 10\sqrt{1 - |ECC|^2} \tag{4}$$

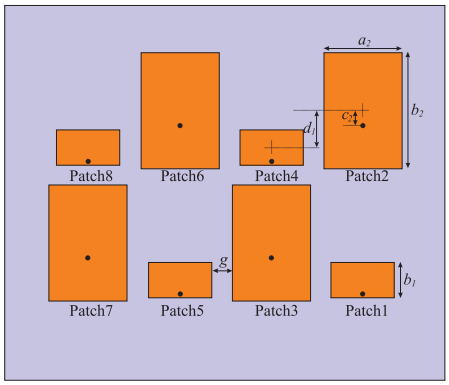

(a)

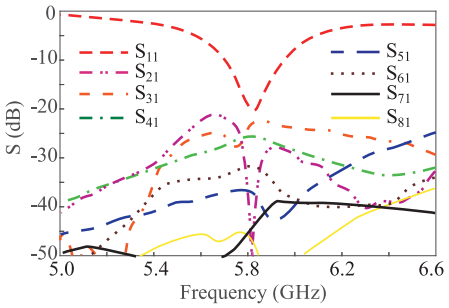

(b)

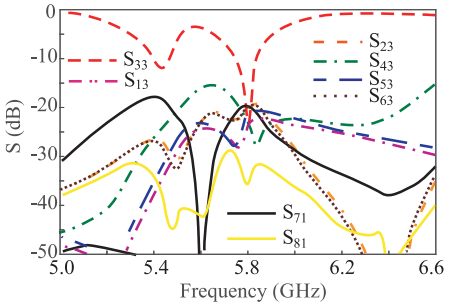

(c)

FIGURE 20. (a) Geometry of the six-element hybrid-plane coupled MIMO antenna array, $[a_2 = 28.2, b_2 = 41.3, c_2 = 9.1, d_1 = 11]_{mm}$, Rest of the design has identical dimensions, as in Fig. 1, (b) *S*-parameters of Patch 1, (c) *S*-parameters of Patch 2.

V. DISCUSSION AND COMPARISON

In the previous designs, the H-plane MPAs were placed side by side, allowing the array to be easily extended to multiple elements H-plane coupled array. In this section, we explore different configurations of the antenna elements further to demonstrate the effectiveness of the proposed isolation technique. To validate this, the 1 × 4 MIMO array was extended to a 2 × 4 MIMO array, as shown in Fig. 20(a) with varied parameters listed in figure caption. Before constructing the 2 × 4 MIMO array, the small-sized MPA and large-sized MPA were arranged in an E-plane configuration, achieving high isolation. However, these results are omitted here for brevity. Nevertheless, the enhancement in isolation for the E-plane and the H-plane elements can be observed in the 2 × 4 MIMO array, with the simulated results for Patch

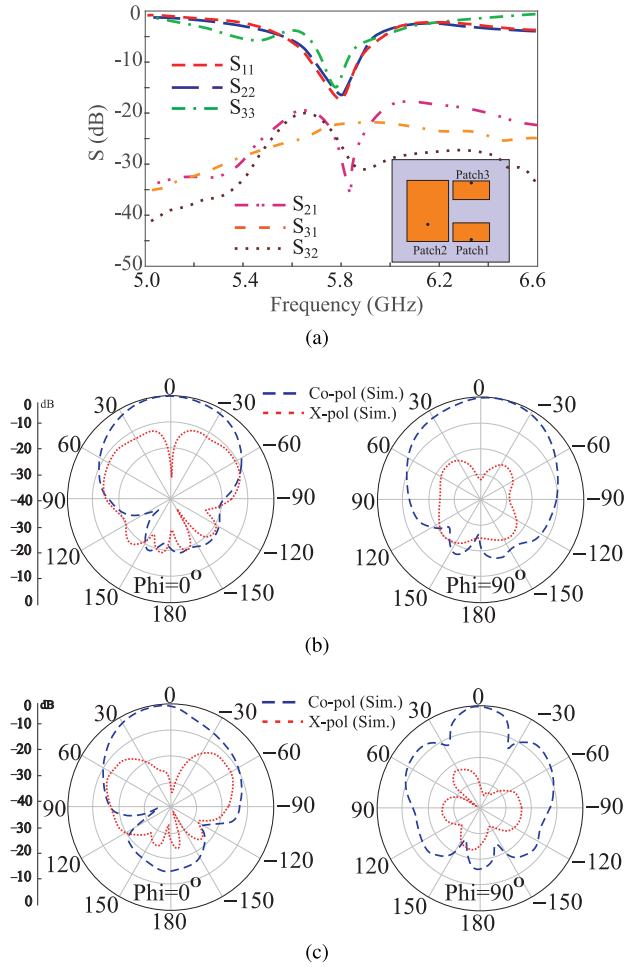

FIGURE 21. Simulated: (a) *S*-parameters of the three element hybrid-plane coupled MIMO array, (b) co-pol and x-pol radiation patterns of Patch 1, (c) co-pol and x-pol radiation patterns of Patch 2.

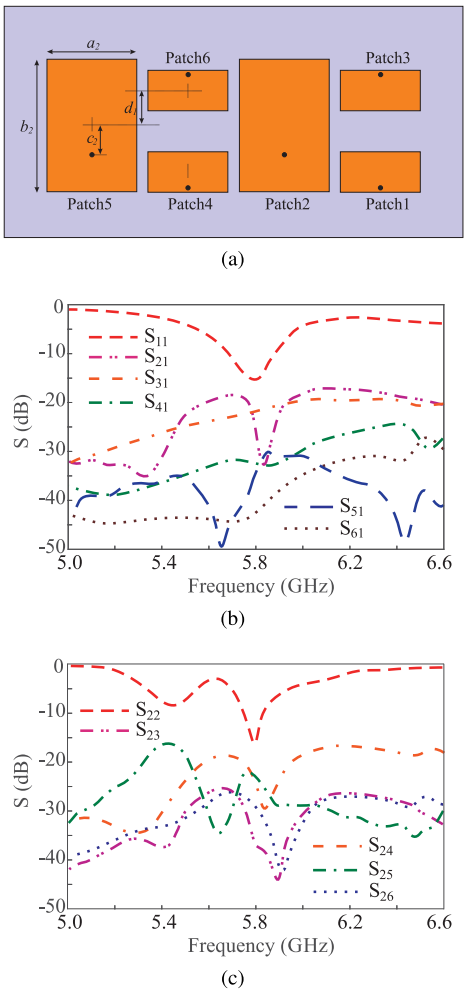

FIGURE 22. (a) Geometry of the six-element hybrid-plane coupled MIMO antenna array, $[a_2 = 28.2, b_2 = 41.3, c_2 = 9.1, d_1 = 11]_{mm}$, Rest of the design has identical dimensions, as in Fig. 1, (b) *S*-parameters of Patch 1, (c) *S*-parameters of Patch 2.

1 and Patch 3 presented in Figs. 20(b) and 20(c), respectively. The isolation among the ports remains greater than 22 dB at 5.8 GHz, demonstrating the robustness of the proposed approach. The simulation results indicate that the array can be extended to an $n \times n$ MIMO array (where $n = 1, 2, 3, \ldots$) with minor optimization of design parameters, further showcasing the scalability and versatility of the proposed technique.

The suggested method has the advantage of using the fundamental mode at the operating frequency to achieve a compact patch size. This configuration saves space, which can be utilized to accommodate additional patch elements. Unlike the two-element array shown in Fig. 1, a third patch is added to the available space to create a three-element MIMO array, as shown in the inset of Fig. 21(a). This approach enables the integration of more elements within a confined area. The third patch, labeled as Patch 3, operates in the fundamental mode and is aligned front-to-front with Patch 1 along the E-plane while being coupled in the H-plane with Patch 2, forming a hybrid-plane coupled MIMO MPA array. All dimensions remain consistent with those provided in Fig. 1. The array elements resonate at 5.8 GHz, achieving an isolation level better than 24 dB, which is suitable for practical purposes. Fig. 21(b) illustrates the simulated radiation patterns of Patch 1, showing a single main lobe and low x-pol levels in the broadside direction in both the $\phi = 0°$ and $\phi = 90°$ planes. Similarly, the radiation patterns of Patch 2 are shown in Fig. 21(c), displaying a single main lobe in the $\phi = 0°$ plane and three lobes in the $\phi = 90°$ plane, as expected. The x-pol levels remain significantly lower than the co-pol levels in both planes. The radiation patterns of Patch 3 are similar to those of Patch 1 and are omitted for brevity. To implement a larger-scale array, a six-element of hybrid configuration can be constructed by replicating the three-port array, as shown in Fig. 22(a). Any modifications to the dimensions in Fig. 1 are listed in the figure caption. The position of Patch 3 and a few additional parameters are adjusted to optimize performance. The *S*-parameters for Patch 1 and Patch 2 are provided in Figs. 22(b) and 22(c), respectively, and the performance of the remaining ports can be inferred accordingly. The patches resonate at 5.8 GHz with

TABLE 1. Comparison of the proposed MPA MIMO antenna array with previous works.

[Ref.]	Decoupling technique.	C–C spacing (λ_0)	Dielectric layers	10 dB IBW(%)	ISL (dB)	η_{peak} (%)	Gain$_{peak}$ (dBi)	X-pol reduction	Merits/Demerits
[14]	Aperture	0.6	3	12.6	20	90	6.5	17	E-, H-plane isolated / complex
[16]	Resonator	0.475	2	9.9	23	92	4.9	–	E-, H-plane isolated / complex, bulky
[18]	Parasitic structure	0.34	1	1.26	18	–	5.5	27, 20	H-plane isolated, simple / large footprint
[22]	Inductance	0.44	2	5.5	13, 15	87	7.8	23	E-plane isolated / bulky
[23]	Mode suppression	0.5	1	1.9	43	96	5.32	<30	E-, H-plane isolated, simple / –
[24]	Out-of-phase modes	0.1	2	11	15	97	6.9	<30	simple/ bulky
[29]	CM of ground plane	0.44	1	7.2	47	–	4.55	30	E-plane isolated, simple / –
[31]	Orthogonal modes	0.4	2	1.7	35	80	5.2	20	E-, H-plane isolated, simple / –
[32]	Field re-distribution	0.5	1	1.8	20	–	10.7	<25	E-, H-plane isolated, simple / –
[Prop.]	Mode diversity	0.5	1	2.9	45	97.5	6.9 ,7.75	40	E-, H-plane isolated, simple / –

C–C: Center to Center, ISL: Isolation

isolation levels exceeding 20 dB among the ports. Based on the designs in Fig. 20 and Fig. 22, the array can be further extended to a higher n^{th}-order configurations with additional optimization.

Table 1 benchmarks the proposed MIMO array design against state-of-the-art MIMO arrays reported in the literature. The table demonstrates that available methods all utilize additional decoupling elements such as aperture [14], resonator [16], parasitic elements [18], and inductance [22], leading to increased design complexity and causing additional insertion loss. Specifically, in [14], an aperture is introduced to provide an alternate coupling path from the feeding line of the excited element to counteract the original coupling. This results in a complex multilayer feeding design. In the same way, a resonator is employed in [16] to add another coupling route to the patch, making the structure more complex. Again, several layers of substrates are required for the transmission line network, resulting in undesirably higher profiles and insertion loss. A grounded parasitic strip is positioned close to the two elements of the MIMO antenna proposed in [18], altering the phase on the coupling patch to minimize mutual coupling. The structure is simple; however, it increases the footprint to a small extent. In [22], a simple inductance is inserted between the E-plane coupled MPAs to tune the impedance of differential modes. Unfortunately, the achieved port isolation is not impressive, only reaching 15 dB.

The table also includes a few self-decoupled MIMO arrays reported in [23], [24], [29], [31], and [32], for a thorough comparison. Although these MIMO MPA arrays also accomplished a satisfactory self-decoupling effect without additional decoupling structures, they exhibit some limitations. For instance, the design in [23] suffers from severe x-pol radiation issues due to the excitation of an orthogonal mode, which is mitigated by etching the slot in the patches. The design in [24] is bulky due to the insertion of an air gap between the ground plane and substrate and it also suffers from low isolation. Similarly, the design in [29] relies strongly on the size of the ground plane. The structure in [31] employs orthogonal modes resulting in high x-pol, whereas the field re-distribution method presented in [32] achieves a low x-pol of 25 dB but suffers mediocre isolation. The proposed MPA MIMO array achieves self-decoupling by employing mode diversity with fundamenal TM_{01} and TM_{03} modes in separate elements at the same frequency. Thus, the technique is very simple, like other self-decoupling methods, without using additional strucutre, and achieve high isolation of 45 dB in the passband. Due to the null creation in the broadside radiation of the coupled modes, the MIMO array has a very low level of x-pol around 40 dB. The proposed design outperforms previous works in terms of both peak gain and efficiency, highlighting its superiority. The peak gains reported in [14], [16], and [18] are lower than those of the proposed design due to the losses introduced by the decoupling structures. While the gain in [22] is higher, this is achieved by including an air gap between the resonator and the ground plane, which makes the design bulky. The proposed design achieves peak gains of 6.9 dBi and 7.75 dBi (depending on the mode), which are higher than those achieved with most other self-decoupling techniques. For instance, [29] (characteristic mode of the ground plane) and [31] (orthogonal mode) achieve gains of 4.55 dBi and 5.2 dBi, respectively, demonstrating limited gain performance of these approaches. Similarly, while [32] achieves a gain of 10.7 dBi by exciting a higher-order mode in the radiator, it does so at the expense of bandwidth and port isolation. In terms of efficiency, the proposed design achieves an exceptional peak efficiency of 97.5%, which is either comparable to or better than other techniques, such as 96% in [23] (mode suppression) and 97% in [24] (out-of-phase modes). This high level of efficiency demonstrates the effectiveness of the mode diversity approach in minimizing energy losses while maintaining superior isolation and reducing x-pol. Unlike other approaches that achieve improvements in gain, efficiency, or isolation at the cost of bulky structures, increased x-pol, high fabrication costs, or compromised performance in other parameters, the proposed design maintains simplicity without sacrificing performance. It offers a balanced trade-off, achieving a rare combination of low x-pol, high isolation, and structural simplicity while maintaining excellent gain and efficiency. These advantages make the proposed design particularly appealing for practical MIMO

applications, where performance and design simplicity are critical. Moreover, the proposed technique applies to both E- and H-plane coupled MIMO arrays.

VI. CONCLUSION

A new self-isolation technique is proposed for a MIMO MPA array, utilizing mode diversity by simultaneously exciting the fundamental TM_{01} mode in one element and the higher-order TM_{03} mode in the other element, both operating at the same frequency. It has been shown that when the excited MPA operates in the TM_{01} mode, a higher-order mode (superposition of TM_{03} and TM_{21}) is excited in the coupled MPA. Similarly, when the other MPA operates in TM_{03} mode, a higher-order TM_{11} mode is excited in the coupled MPA. In both cases, the higher-order or superposed mode's fields are made weak at the feeding point, thereby reducing the mutual coupling between the two elements without the need for an additional decoupling structure. This results in over 50 dB isolation in a 1×2 MIMO configuration. In addition, the coupled modes generate nulls in the broadside direction, significantly reducing the x-pol radiation. The technique was further validated through a 1×4 MIMO array, which demonstrated isolation levels ranging from 30 to 45 dB across the passband, along with a low x-pol level of approximately 40 dB in the broadside direction. This design approach provides a geometrically simple yet effective solution for enhancing MIMO antenna performance. The space saved by this method has been utilized to accommodate a third patch, increasing the number of MIMO elements within a confined space. Additionally, it has been demonstrated that this method is effective for both E-plane and H-plane coupled MIMO arrays by constructing a 2×4 MIMO array, validating its scalability for larger array implementations. The proposed decoupling method has also been successfully applied to MIMO DRA systems, showing effectiveness in both isolation and radiation performance. These traits make the design a promising candidate for wireless communication systems.

REFERENCES

[1] M. A. Jensen and J. W. Wallace, "A review of antennas and propagation for MIMO wireless communications," *IEEE Trans. Antennas Propag.*, vol. 52, no. 11, pp. 2810–2824, Nov. 2004.

[2] À. O. Martínez, J. Ø. Nielsen, E. De Carvalho, and P. Popovski, "An experimental study of massive MIMO properties in 5G scenarios," *IEEE Trans. Antennas Propag.*, vol. 66, no. 12, pp. 7206–7215, Dec. 2018.

[3] X. Chen, S. Zhang, and Q. Li, "A review of mutual coupling in MIMO systems," *IEEE Access*, vol. 6, pp. 24706–24719, 2018.

[4] G. M. Battaglia, T. Isernia, R. Palmeri, and A. F. Morabito, "Synthesis of orbital angular momentum antennas for target localization," *Radio Sci.*, vol. 58, no. 2, pp. 1–15, Feb. 2023.

[5] M. Elahi, J. Joung, and S. Lim, "Isolation and bandwidth enhancement in compact CP MIMO DRA in H-plane using Z-shaped strip," *IEEE Antennas Wireless Propag. Lett.*, vol. 22, no. 11, pp. 2700–2704, Nov. 2023.

[6] M. Elahi, A. Altaf, E. Almajali, and J. Yousaf, "Mutual coupling reduction in closely spaced MIMO dielectric resonator antenna in H-plane using closed metallic loop," *IEEE Access*, vol. 10, pp. 71576–71583, 2022.

[7] J. Xu, W. Hong, Z. H. Jiang, and H. Zhang, "Wideband, low-profile patch array antenna with corporate stacked microstrip and substrate integrated waveguide feeding structure," *IEEE Trans. Antennas Propag.*, vol. 67, no. 2, pp. 1368–1373, Feb. 2019.

[8] B. Qian, X. Chen, L. Zhao, J. Chen, and A. A. Kishk, "Reduced cross-polarization and backside radiations for rectangular microstrip antennas using defected ground structure combined with decoupling structure," *IEEE Antennas Wireless Propag. Lett.*, vol. 22, pp. 517–521, 2023.

[9] D. Gao, Z.-X. Cao, S.-D. Fu, X. Quan, and P. Chen, "A novel slot-array defected ground structure for decoupling microstrip antenna array," *IEEE Trans. Antennas Propag.*, vol. 68, no. 10, pp. 7027–7038, Oct. 2020.

[10] X. Tan, W. Wang, Y. Wu, Y. Liu, and A. A. Kishk, "Enhancing isolation in dual-band meander-line multiple antenna by employing split EBG structure," *IEEE Trans. Antennas Propag.*, vol. 67, no. 4, pp. 2769–2774, Apr. 2019.

[11] Z. Qamar, U. Naeem, S. A. Khan, M. Chongcheawchamnan, and M. F. Shafique, "Mutual coupling reduction for high-performance densely packed patch antenna arrays on finite substrate," *IEEE Trans. Antennas Propag.*, vol. 64, no. 5, pp. 1653–1660, May 2016.

[12] H. Qi, X. Yin, L. Liu, Y. Rong, and H. Qian, "Improving isolation between closely spaced patch antennas using interdigital lines," *IEEE Antennas Wireless Propag. Lett.*, vol. 15, pp. 286–289, 2016.

[13] H. Nguyen-Manh, D.-P. Pham, G. Nguyen-Hoai, H.-H. Tran, and N. Q. Dinh, "A design of MIMO antenna with high isolation and compact size characteristics," *IEEE Access*, vol. 11, pp. 93948–93955, 2023.

[14] Y.-M. Zhang and S. Zhang, "A novel aperture-loaded decoupling concept for patch antenna arrays," *IEEE Trans. Microw. Theory Techn.*, vol. 69, no. 9, pp. 4272–4283, Sep. 2021.

[15] W. Song, X.-W. Zhu, L. Wang, and W. Hong, "Simple structure E-plane decoupled millimeter wave antenna based on current cancellation model," *IEEE Trans. Antennas Propag.*, vol. 70, no. 10, pp. 9871–9876, Oct. 2022.

[16] Y.-F. Cheng and K. M. Cheng, "Decoupling of 2×2 MIMO antenna by using mixed radiation modes and novel patch element design," *IEEE Trans. Antennas Propag.*, vol. 69, no. 12, pp. 8204–8213, Dec. 2021.

[17] M. Li and S. Cheung, "Isolation enhancement for MIMO dielectric resonator antennas using dielectric superstrate," *IEEE Trans. Antennas Propag.*, vol. 69, no. 7, pp. 4154–4159, Jul. 2021.

[18] T. Pei, L. Zhu, J. Wang, and W. Wu, "A low-profile decoupling structure for mutual coupling suppression in MIMO patch antenna," *IEEE Trans. Antennas Propag.*, vol. 69, no. 10, pp. 6145–6153, Oct. 2021.

[19] J. Fang, J. Li, P. Xiao, J. Dong, G. Li, S. Du, and W. T. Joines, "Coupling mode transformation-based dielectric surface and metasurface for antenna decoupler," *IEEE Trans. Antennas Propag.*, vol. 71, no. 1, pp. 1123–1128, Jan. 2023.

[20] A. Jafargholi, A. Jafargholi, and J. H. Choi, "Mutual coupling reduction in an array of patch antennas using CLL metamaterial superstrate for MIMO applications," *IEEE Trans. Antennas Propag.*, vol. 67, no. 1, pp. 179–189, Jan. 2019.

[21] M. Li, B. G. Zhong, and S. W. Cheung, "Isolation enhancement for MIMO patch antennas using near-field resonators as coupling-mode transducers," *IEEE Trans. Antennas Propag.*, vol. 67, no. 2, pp. 755–764, Feb. 2019.

[22] L. Sun, Y. Li, and Z. Zhang, "Decoupling between extremely closely spaced patch antennas by mode cancellation method," *IEEE Trans. Antennas Propag.*, vol. 69, no. 6, pp. 3074–3083, Jun. 2021.

[23] Q. X. Lai, Y. M. Pan, S. Y. Zheng, and W. J. Yang, "Mutual coupling reduction in MIMO microstrip patch array using TM_{10} and TM_{02} modes," *IEEE Trans. Antennas Propag.*, vol. 69, no. 11, pp. 7562–7571, Nov. 2021.

[24] K.-L. Wong, M.-F. Jian, C.-J. Chen, and J.-Z. Chen, "Two-port same-polarized patch antenna based on two out-of-phase TM_{10} modes for access-point MIMO antenna application," *IEEE Antennas Wireless Propag. Lett.*, vol. 20, pp. 572–576, 2021.

[25] J. Sui, Y. Dou, X. Mei, and K.-L. Wu, "Self-curing decoupling technique for MIMO antenna arrays in mobile terminals," *IEEE Trans. Antennas Propag.*, vol. 68, no. 2, pp. 838–849, Feb. 2020.

[26] J. Sui and K.-L. Wu, "Self-curing decoupling technique for two Inverted-F antennas with capacitive loads," *IEEE Trans. Antennas Propag.*, vol. 66, no. 3, pp. 1093–1101, Mar. 2018.

[27] Q. Xuan Lai, Y. Mei Pan, and S. Yong Zheng, "Mode-counteraction based self-decoupling in circularly polarized MIMO microstrip patch array," *IEEE Trans. Antennas Propag.*, vol. 70, no. 10, pp. 9337–9346, Oct. 2022.

[28] Q. X. Lai and Y. Mei Pan, "Self-decoupled MIMO circularly polarized dielectric resonator antenna array using higher-order mode," in *Proc. IEEE Int. Symp. Antennas Propag. USNC-URSI Radio Sci. Meeting (AP-S/URSI)*, Jul. 2022, pp. 13–14.

[29] Q. X. Lai, Y. M. Pan, and S. Y. Zheng, "A self-decoupling method for MIMO antenna array using characteristic mode of ground plane," *IEEE Trans. Antennas Propag.*, vol. 71, no. 3, pp. 2126–2135, Mar. 2023.

[30] L. Sun, H. Feng, Y. Li, and Z. Zhang, "Compact 5G MIMO mobile phone antennas with tightly arranged orthogonal-mode pairs," *IEEE Trans. Antennas Propag.*, vol. 66, no. 11, pp. 6364–6369, Nov. 2018.
[31] P. Kim-Thi, T. Nguyen Van, and T. Bui Thanh, "A self-decoupling technique for isolation enhancement in closely-spaced MIMO patch antennas," *IEEE Antennas Wireless Propag. Lett.*, vol. 23, pp. 1695–1699, 2024.
[32] K.-D. Hong, X. Zhang, H.-Y. Weng, L. Zhu, and T. Yuan, "A 2-D self-decoupling method based on antenna-field redistribution for MIMO patch antenna array," *IEEE Antennas Wireless Propag. Lett.*, vol. 23, pp. 940–944, 2024.
[33] C. A. Balanis, *Antenna Theory: Analysis and Design*. Hoboken, NJ, USA: Wiley, 2015.
[34] R. Kumar Mongia and A. Ittipiboon, "Theoretical and experimental investigations on rectangular dielectric resonator antennas," *IEEE Trans. Antennas Propag.*, vol. 45, no. 9, pp. 1348–1356, Sep. 1997.
[35] M. Elahi, A. Altaf, Y. Yang, K.-Y. Lee, and K. C. Hwang, "Circularly polarized dielectric resonator antenna with two annular vias," *IEEE Access*, vol. 9, pp. 41123–41128, 2021.
[36] Y.-M. Pan, K. W. Leung, and K.-M. Luk, "Design of the millimeter-wave rectangular dielectric resonator antenna using a higher-order mode," *IEEE Trans. Antennas Propag.*, vol. 59, no. 8, pp. 2780–2788, Aug. 2011.
[37] M. Elahi, S. Koziel, and L. Leifsson, "A Non-PCM-based 2×2 MIMO antenna array with low radar cross-section using characteristic mode analysis," *IEEE Access*, vol. 13, pp. 34296–34306, 2025.

MANZOOR ELAHI received the M.S. degree in electrical engineering from COMSATS University Islamabad, Pakistan, in 2015, and the Ph.D. degree in electrical engineering from Sungkyunkwan University, Suwon, South Korea. Before pursuing the Ph.D. degree, he was a Lecturer with the Department of Electrical and Computer Engineering, COMSATS University Islamabad. He is currently a Postdoctoral Researcher with the Department of Engineering, Reykjavik University, Iceland. Previously, he was a Postdoctoral Researcher with the Department of Electrical Engineering, Chung-Ang University, Seoul, South Korea. His research interests include MIMO antennas, circularly polarized antennas, reconfigurable dielectric resonator antennas, metasurfaces, and reflectarray antennas.

SLAWOMIR KOZIEL (Senior Member, IEEE) received the M.Sc. and Ph.D. degrees in electronic engineering from Gdańsk University of Technology, Poland, in 1995 and 2000, respectively, and the first M.Sc. degree in theoretical physics and the second M.Sc. and Ph.D. degrees in mathematics from the University of Gdańsk, Poland, in 2000, 2002, and 2003, respectively. He is currently a Professor with the Department of Engineering, Reykjavik University, Iceland. His research interests include CAD and modeling of microwave and antenna structures, simulation-driven design, surrogate-based optimization, space mapping, circuit theory, analog signal processing, evolutionary computation, and numerical analysis.

LEIFUR LEIFSSON received the bachelor's and master's degrees in mechanical engineering from the University of Iceland, Reykjavik, Iceland, in 1999 and 2000, respectively, and the Ph.D. degree in aerospace engineering from Virginia Tech, Blacksburg, VA, USA, in 2006. He is currently an Associate Professor of aerospace engineering with Purdue University, West Lafayette, IN, USA. His research interests include computational modeling, optimization, and uncertainty quantification of engineered systems with an emphasis on methods for multifidelity modeling and machine learning. His current application areas include aerodynamic shape optimization, aerodynamic flutter, model-based nondestructive evaluation, microwave devices, and food-energy-water nexus.